Physics

Physics Research Publications

Purdue University *Year* 2011

Correlation of fermi photons with high-frequency radio giant pulses from the crab pulsar

A. V. Bilous* V. I. Kondratiev† M. A. McLaughlin‡

S. M. Ransom** M. Lyutikov††

M. Mickaliger‡‡ G. I. Langston§

*

†

‡

**

††

‡‡

§

The Astrophysical Journal, 728:110 (8pp), 2011 February 20 doi:10.1088/0004-637X/728/2/110

CORRELATION OF *FERMI* PHOTONS WITH HIGH-FREQUENCY RADIO GIANT PULSES FROM THE CRAB PULSAR

A. V. Bilous[1], V. I. Kondratiev[2,3], M. A. McLaughlin[4,5], S. M. Ransom[6], M. Lyutikov[7], M. Mickaliger[4], and G. I. Langston[5]

[1] Department of Astronomy, University of Virginia, P.O. Box 400325, Charlottesville, VA 22904, USA; avb3k@virginia.edu
[2] Netherlands Institute for Radio Astronomy (ASTRON), Postbus 2, 7990 AA Dwingeloo, The Netherlands; kondratiev@astron.nl
[3] Astro Space Center of the Lebedev Physical Institute, Profsoyuznaya str. 84/32, Moscow 117997, Russia
[4] Department of Physics, West Virginia University, Morgantown, WV 26506, USA
[5] National Radio Astronomy Observatory, Green Bank, WV 24944, USA
[6] National Radio Astronomy Observatory, Charlottesville, VA 22903, USA
[7] Department of Physics, Purdue University, West Lafayette, IN 47907, USA
Received 2010 November 18; accepted 2010 December 14; published 2011 January 26

ABSTRACT

To constrain the giant pulse (GP) emission mechanism and test the model of Lyutikov for GP emission, we have carried out a campaign of simultaneous observations of the Crab pulsar at γ-ray (*Fermi*) and radio (Green Bank Telescope) wavelengths. Over 10 hr of simultaneous observations we obtained a sample of 2.1×10^4 GPs, observed at a radio frequency of 9 GHz, and 77 *Fermi* photons, with energies between 100 MeV and 5 GeV. The majority of GPs came from the interpulse (IP) phase window. We found no change in the GP generation rate within 10–120 s windows at lags of up to $\pm$40 minutes of observed γ-ray photons. The 95% upper limit for a γ-ray flux enhancement in pulsed emission phase window around all GPs is four times the average pulsed γ-ray flux from the Crab. For the subset of IP GPs, the enhancement upper limit, within the IP emission window, is 12 times the average pulsed γ-ray flux. These results suggest that GPs, at least high-frequency IP GPs, are due to changes in coherence of radio emission rather than an overall increase in the magnetospheric particle density.

Key words: gamma rays: stars – pulsars: individual (B0531+21)

1. INTRODUCTION

The Crab pulsar was discovered by Staelin & Reifenstein III in 1968 by its remarkably bright giant pulses (GPs). GPs are short (from few ns to few μs), sporadic bursts of pulsar radio emission (Popov & Stappers 2007; Hankins et al. 2003). The nature of GPs is far from being clear and even the precise definition of GP had not yet been given (Knight et al. 2006). GPs generally occur only in certain narrow ranges of pulse phase that are often coincident with pulses seen at X-ray and γ-ray energies (Lundgren 1994). Popov et al. (2006) propose that all radio emission from the Crab (except for that in the precursor) is composed entirely of GPs, consistent with the alignment of the GP and high-energy components seen in other pulsars exhibiting GPs (Cusumano et al. 2003; Knight et al. 2006).

The Crab pulsar shows pulsed emission across the entire electromagnetic spectrum (see Figure 1, left), reflecting different radiation processes in the pulsar magnetosphere—from coherent curvature or synchrotron (radio) to incoherent synchrotron (optical and X-ray) and incoherent curvature (γ-ray) radiation. Similar to other sporadic variability phenomena seen in pulsar radio emission, represented by nulling pulsars (e.g., Herfindal & Rankin 2009), intermittent pulsars (Kramer et al. 2006), and rotating radio transients (McLaughlin et al. 2006), GP emission could be due to changes in the coherence of the radio emission, variations in the pair creation rate in the magnetosphere, or changes in the beaming direction. If the GP phenomenon is due to changes in the coherence of the radio emission mechanism, then one would expect little correlation of the radio GPs with the high-energy emission. However, if the GPs are due to changes in the actual rate of pair creation in the pulsar magnetosphere, one would expect an increased flux at high energies at the time of the GPs. Similarly, because the radio GP and γ-ray components are aligned, one expects that they come from the same place in the pulsar magnetosphere. Therefore, if a GP occurs from a beam direction alteration, one would expect to also see an increase in the high-energy flux.

Lundgren et al. (1995) previously attempted to carry out simultaneous radio/γ-ray observations (50–220 keV, the energy range of *CGRO*/OSSE) and correlate times of arrival (TOAs) of GPs at 800 and 1300 MHz with γ-ray photons. Their upper limit on the γ-ray flux increase concurrent with radio GPs was $\leqslant$2.5. Later, Ramanamurthy & Thompson (1998) correlated the same set of GPs with EGRET photons of energy $>$50 MeV, placing an upper limit on concurrent γ-ray flux of 4.6 times the average Crab flux. This suggested that the GP mechanism is largely based on changes in coherence and not changes in pair production rates or beaming. Yet, Shearer et al. (2003) performed simultaneous radio/optical observations of the Crab pulsar and found a weak correlation, i.e., that optical pulses coincident with radio GPs were on average 3% brighter than others. This observation suggested that the GP emission mechanism, whatever its nature, includes small variations in magnetospheric particle density.

Lyutikov (2007) proposed a more specific, quantitative model of GP emission in which Crab GPs are generated on closed magnetic field lines near the light cylinder via anomalous cyclotron resonance on the ordinary mode. During emission of a photon, an electron undergoes transition up in Landau levels. The energy is supplied by the parallel motion (Ginzburg 1985). The application of anomalous cyclotron resonance to pulsar radio emission has been discussed by Lyutikov et al. (1999) and Machabeli & Usov (1979).

One clear prediction of this model is that radio GPs (at least those at radio frequencies $>$4 GHz) should be accompanied by γ-ray photons, as the high-energy beam is expected to produce curvature radiation at energies $\sim \hbar\gamma^3\Omega \sim$ 0.1–100 GeV, depending on the exact value of the Lorentz factor γ. These

energies fall into the energy range of the *Fermi* mission, and so this hypothesis can also be tested through high-frequency radio observations concurrent with *Fermi*.

The *Fermi* Large Area Telescope (LAT), with its large effective area, broad field of view, and superior angular resolution, is a perfect tool for testing the Lyutikov theory and investigating the possible correlation between GPs and γ-ray photons in general. For the radio observations, using the 100 m Green Bank Telescope (GBT) allows one to record a very large number of GPs within a reasonable observing time, even at frequencies above 4 GHz. Thus, a thorough study of the correlation between high-energy γ-ray photons and high-frequency GPs is possible.

In this paper, we present the results of simultaneous GBT/LAT observations of the Crab pulsar. To probe the level of correlation between GPs and γ-ray photons, we used two main approaches. First, we searched for a "burst correlation" by examining whether GPs tend to cluster near γ-ray photons. Second, we analyzed whether the average γ-ray flux of the pulsar increases within the pulse phase windows where single GPs are produced.

In Sections 2 and 3 below we describe the radio observations and *Fermi* data used in this analysis. Section 4 discusses the influence of the interstellar medium (ISM) on the observed GP sample. We describe the correlation analysis between radio GPs and *Fermi* photons in Section 5, and conclude in Section 6.

2. RADIO OBSERVATIONS

The radio observations were carried out during 12 observing sessions in 2009 September–October with the GBT, using the new Green Bank Ultimate Pulsar Processor Instrument (GUPPI) at a central frequency of 8.9 GHz, in incoherent dedispersion mode. The total bandwidth of 800 MHz was split into 256 frequency channels, and the total intensity was recorded with a sampling interval 2.56–3.84 μs. Total observing time was $\sim$26 hr or $\sim 3 \times 10^6$ pulsar periods.

The raw data from every session were dedispersed with the current dispersion measure of the Crab pulsar[8] using the PRESTO package,[9] and searched for all single-pulse events with signal-to-noise ratio (S/N) > 7. Since GPs from the Crab pulsar do not have any established lower limit on peak flux density (Popov et al. 2006), we picked up initial threshold of S/N > 7 in order not to contaminate our sample by numerous spurious detections on noise. Each event was assigned a width, found by averaging the dedispersed time series with different numbers of samples and finding the number that resulted in a peak in S/N. The list of event times was put into TEMPO2 format (Hobbs et al. 2006) and converted to the barycentric reference frame for the correlation analysis with *Fermi* data. TOAs were corrected for delay due to propagation in the ionized ISM.

Estimated timing errors due to an inaccurate DM are less than our time resolution, assuming that DM varies smoothly and that between observing sessions the change in DM is less than the change over two months. For $\mathrm{DM_{Oct}}$–$\mathrm{DM_{Sep}} = 0.0104$ pc cm^{-3}, timing errors are about 0.5 μs.

Figure 1 (right) shows the average pulse profile (top) of the Crab pulsar at 8.9 GHz together with the subintegrations from one of the two subsessions on 2009 September 25, which had the highest rate of GP detection of all 12 sessions. The interpulse (IP) and high-frequency components (HFCs) are clearly seen, with the weak peak after HFC2 being the main pulse (MP). However, on September 25 the pulsar was the brightest, and during other sessions the average profile was less prominent. During some sessions, we did not accumulate a detectable average profile at all.

The system equivalent flux density (SEFD) is mostly determined by the Crab Nebula. Flux densities for the Crab Nebula were calculated with the relation $S(f) = 955 \times (f/\mathrm{GHz})^{-0.27}$ Jy (Cordes et al. 2004), accounting for the fact that at 8.9 GHz the solid angle of the GBT beam covers only 25% of the area occupied by the nebula. We estimate a SEFD $= 1.3/\sqrt{\Delta t/1\ \mu\mathrm{s}}$ Jy, or about 0.7 Jy for our most common sampling time, or Δt, of 3.2 μs.

Preliminary analysis of all events with S/N > 7 revealed that GPs appear mostly in the MP and IP phase windows. Only for two observing sessions, namely, on September 25 and 28, were there several GPs detected in the HFCs, all with S/N close to 9. This is to some extent surprising, since Jessner et al. (2005) observed the Crab pulsar with similar parameters and timespan, and found about 120 GPs in HFCs versus 350 GPs in the MP and IP. However, their threshold peak flux density of 25 Jy was much higher than our threshold of about 6 Jy, suggesting that the GPs from HFCs are rarer but brighter.

Some of our sessions were heavily contaminated with broad radio frequency interference (RFI) pulses with typical S/N < 10. Therefore, we analyzed only events with a peak flux density exceeding 8.1 Jy (S/N $= 10$ for the session with smallest sampling time) and which arrived in the MP or IP phase windows. Additionally, we excluded all events with width larger than 30 sample intervals, as being presumably caused by RFI. These cuts resulted in the selection of more than 40,000 GPs. Comparing the number of single pulses above 8.1 Jy and narrower than 30 samples in and out of the pulsed emission phase windows, we can estimate the proportion of false GPs in our final data set to be less than 0.001%.

The summary of observations is given in Table 1. For each observing date the listed columns are: time resolution, SEFD, total duration of radio observations and the time simultaneous with *Fermi*, number of GPs, detected during the whole observing session and during the time simultaneous with *Fermi*, and the number of γ-ray photons selected for further analysis (see Section 3).

3. *FERMI* DATA

We extracted "Diffuse" class events with energies from 100 MeV to 300 GeV from the *Fermi* database, concurrent with each radio observation. Photons with zenith angles greater than 105° were excluded to eliminate the γ-rays generated in the Earth's atmosphere.

We selected only photons in Good Time Intervals (GTIs) within an angle $\theta < \mathrm{Max}(6.68\text{–}1.76\log(E/1000\ \mathrm{MeV}), 1.3)^\circ$ of the radio pulsar position (Abdo et al. 2010). Photon arrival times were converted to the solar system barycenter and assigned phases with the TEMPO2 `fermi` plugin. The timing accuracy of the *Fermi* LAT is better than 1 μs (Abdo et al. 2010). LAT dead time per event is less than 100 μs,[10] which is less than 3% of pulsar rotational phase. Over the course of all radio observations we accumulated 10.5 hr of *Fermi* data within GTIs, resulting in 77 photons with energies above 100 MeV (see Table 1).

[8] The DM was 56.8005 pc cm^{-3} for September and 56.8109 pc cm^{-3} for October, from the Jodrell Bank Crab pulsar monthly ephemeris: http://www.jb.man.ac.uk/pulsar/crab.html.

[9] http://www.cv.nrao.edu/~sransom/presto/

[10] The dead time was taken from *Fermi* Technical Handbook, http://fermi.gsfc.nasa.gov/ssc/proposals/manual/.

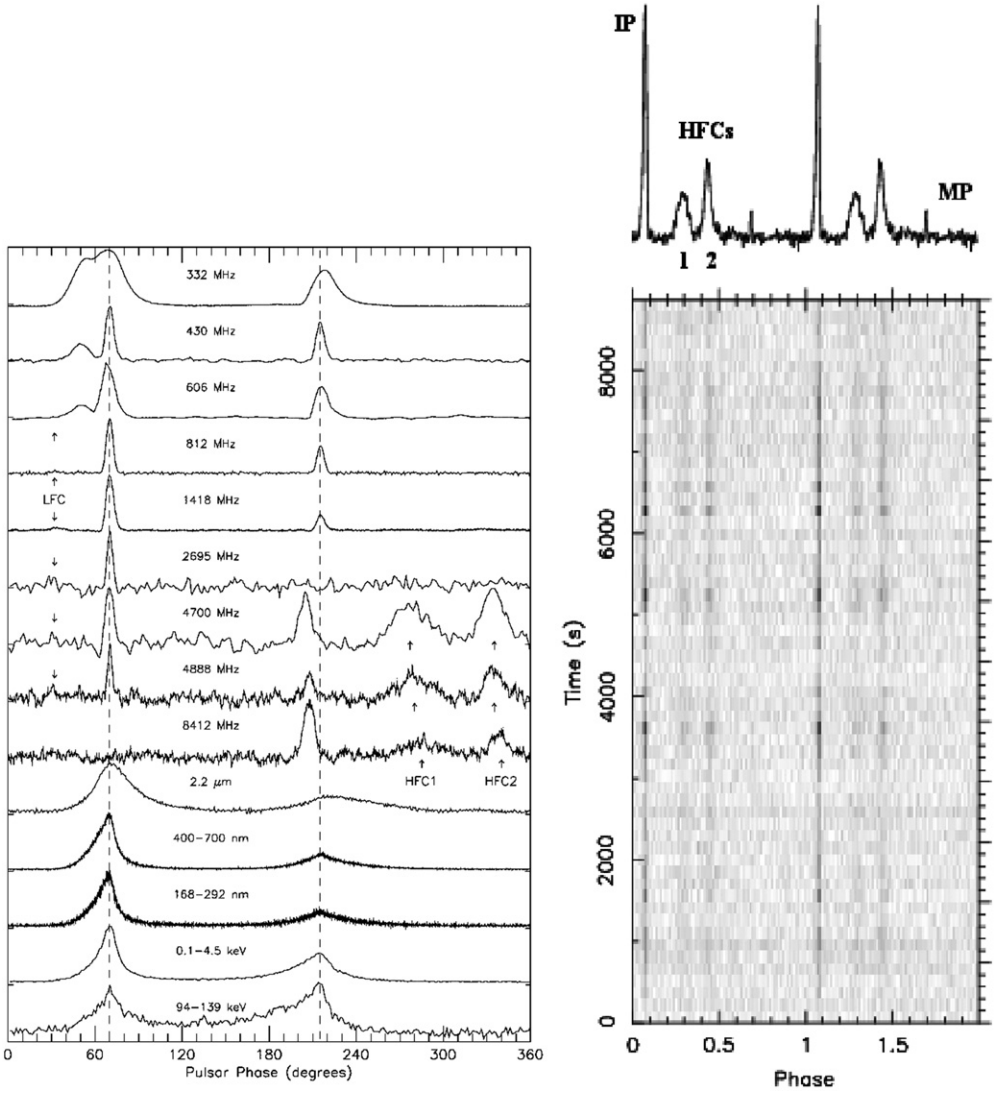

Figure 1. Left: average profile of the Crab pulsar from radio to γ-rays, from the paper of Moffett & Hankins (1996). Right: average Crab pulsar radio profile for one out of two subsessions with the GBT on 2009 September 25.

Figure 2 gives a quick visual summary of our simultaneous observations, showing *Fermi* photons and radio GPs versus observing time for each session. The distribution of number and energy/peak intensity of photons/GPs with respect to pulsar rotational phase is shown in Figure 3. As reported earlier, γ-ray and radio emission windows are aligned.

4. PROPAGATION EFFECTS FOR GIANT PULSES

At high frequencies, GPs are strongly affected by interstellar scintillations (Cordes et al. 2004), which change their apparent rate and peak intensities. Careful treatment of ISM effects is crucial for a proper correlation analysis. Unfortunately, we did not make direct measurements of typical ISM diagnostic parameters, such as scintillation bandwidth and pulse broadening time. Instead, we use the scintillation timescales scaled from other frequencies. These values give only a rough estimate of scintillation timescales at 8.96 GHz, since for the Crab pulsar the main contribution to scintillations is made by the turbulent and quickly changing Crab Nebula. Scintillation parameters for the Crab have been shown to be strongly variable with time (see Cordes et al. 2004, and references therein).

The refractive interstellar scintillation (RISS) timescale, $\tau_{\rm RISS}$, can be scaled using the $\nu^{-2.2}$ dependence derived from a five frequency data set (Rickett & Lyne 1990). At 8.96 GHz, $\tau_{\rm RISS}$ is about 80 minutes, thus roughly matching the observed day-to-day variation of the GP rate (see Figure 2). Also, for the longest, 4 hr session, note the change of GP rate between two 2 hr scans in Figure 2 (observing settings were the same for both scans).

Following Cordes et al. (2004), for calculating the diffractive interstellar scintillation (DISS) timescale, $\tau_{\rm DISS}$, we adopted the thin screen model with a Kolmogorov spectrum of irregularities and reference pulse broadening time $\tau_d = 0.5$ ms at 0.3 GHz. At 8.9 GHz, with bandwidth of 800 MHz, this gives us a scintillation strength $u = 8.9$, well into the strong scintillation regime, and $\tau_{\rm DISS} = \tau_{\rm RISS}/u^2 \simeq 9$ minutes.

The variation of the GP rate within each observing subsession was estimated by autocorrelating the rate of GP emission in 10 s bins. The autocorrelation analysis shows two shorter GP rate variability timescales of ~20 minutes and 2–4 minutes. Both of them agree fairly well with the DISS estimations, considering all the uncertainty in the scintillation parameters. On the other hand, there is no evidence against the hypothesis

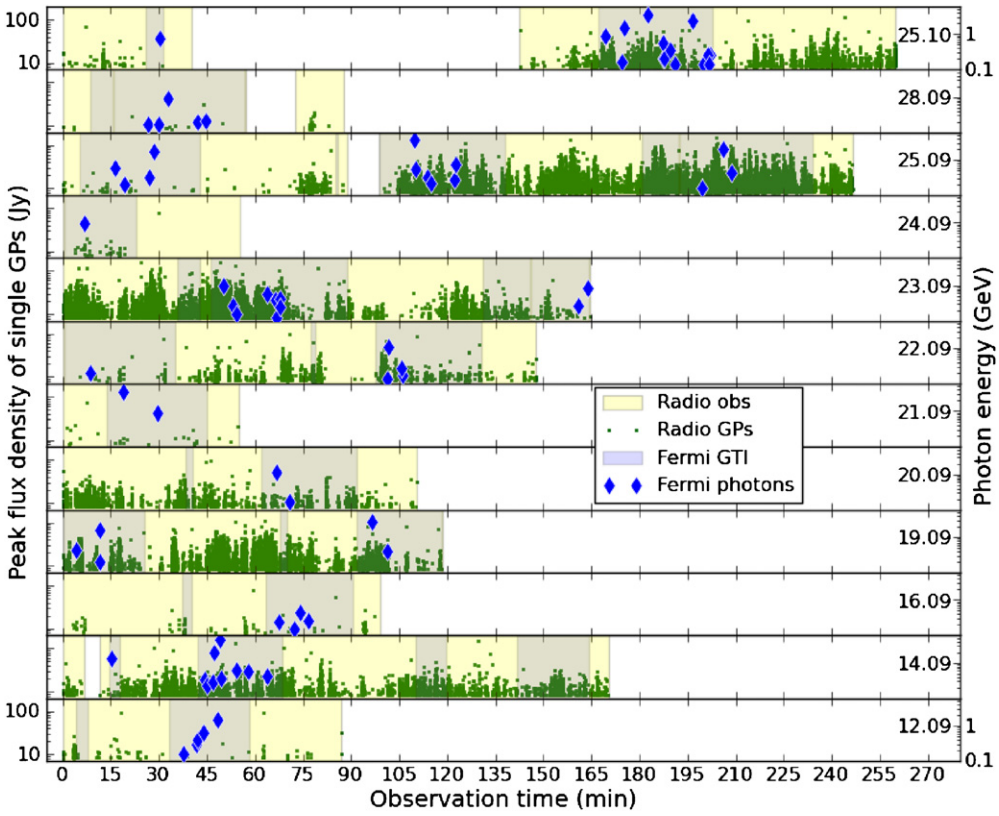

Figure 2. Time series of radio GPs and *Fermi* photons during 12 observing sessions. *X*-axis: time from the beginning of each session, in minutes. *Y*-axis (left): peak flux density of radio GPs. *Y*-axis (right): energy of γ-ray photons. Both scales are the same for each observing session. The yellow shaded regions mark the time when we actually were recording radio data and the blue are the *Fermi* Good Time Intervals. The observing date is given in the upper right-hand corner of each subplot. For the observing session on October 25 two photons came within a short time interval, so their markers overlap and one can see only 14 photons, instead of 15.

Table 1
Summary of Observational Parameters and GP/γ-ray Outcome for Each Observing Date

Date	Δt	SEFD	Radio Time		$N_{\rm GPs}$		N_γ
			Total	With *Fermi*	All	With	
(2009)	(μs)	(Jy)	(minutes)	(minutes)		*Fermi*	
Sep 12	2.56	0.81	87.1	28.9	139	8	5
Sep 14	3.20	0.73	165.7	62.1	4375	1834	10
Sep 16	3.84	0.66	99.3	30.6	98	27	4
Sep 19	3.20	0.73	118.5	54.3	6957	1830	5
Sep 20	3.20	0.73	110.5	32.2	1846	384	2
Sep 21	3.84	0.66	55.1	31.5	27	16	2
Sep 22	3.20	0.73	147.7	68.9	1256	603	5
Sep 23	3.20	0.73	164.5	82.0	10520	5078	10
Sep 24	3.84	0.66	55.3	22.5	38	37	1
Sep 25	3.20	0.73	236.5	130.8	14320	10014	13
Sep 28	3.20	0.73	72.3	48.1	34	9	5
Oct 25	3.20	0.73	157.6	41.3	3164	1261	15
Total			1470.0	633.1	42774	21092	77

Notes. Columns include (from left to right): date of observation, time resolution, system equivalent flux density (SEFD), total duration of radio observations and the time simultaneous with *Fermi*, number of giant pulses, $N_{\rm GPs}$, detected during the whole observing session and during the time simultaneous with *Fermi*, number of γ-ray photons, N_γ.

that at least one of these timescales is due to intrinsic GP rate variability.

The following analysis assumes that observed day-to-day variation (or, in the case of September 25, variation between two subsessions) of the GP rate and mean intensity is caused by RISS. If intrinsic GP rate and mean intensity are constant on timescales larger than 90 minutes, then it is relatively easy to make a GP sample corrected for refractive scintillation. We accomplish this by estimating the amount of RISS intensity damping on each observation session with respect to the session with the highest GP rate. Then, we multiplied the intensities of all pulses in each separate session by those amounts, and threw out all GPs below a threshold, common for the corrected GPs over all sessions.

A simple way to calculate the intensity variation due to RISS would be by comparing mean profiles of pulsed emission accumulated during each session. However, at these frequencies, our observations were not sensitive enough to accumulate the normal Crab pulse profile except on one or two sessions where scintillations caused a boosting of the average flux density of the pulsar. Instead, we compared the intensity distributions of GPs between sessions. If the change in rate and mean intensity of GPs on timescales of a few hours is due to RISS, then the peak intensity distributions for each day should have the same shape, but with different values of peak flux density. The distributions in Figure 4 (left) show that this assumption is basically correct.

As the reference session, we picked the one with the highest rate of GPs, the second subsession of September 25 (from now on called "0925/2" or "reference session"). For each day and for the two subsessions on September 25 separately, we determined the RISS damping coefficient, k, by minimizing χ^2:

$$\chi^2_k = \frac{1}{N_{\rm bins}-1}\sum_{I_i}\frac{[N_{\rm ref}(I_i) - N(I_i/k)]^2}{\sigma^2_{N(I_i/k)}}, \qquad (1)$$

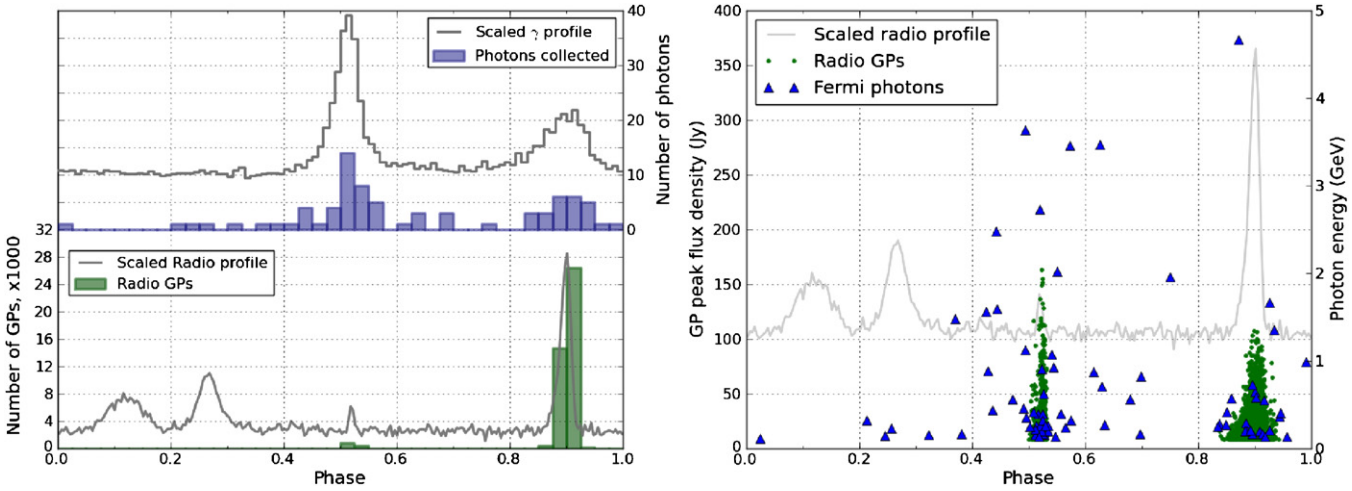

Figure 3. Left: histograms of GPs for all radio observing time (bottom) and *Fermi* photons during the simultaneous time (top). For illustrative purposes, scaled radio and γ-ray profiles (gray) are shown with arbitrary offset along the y-axis. The scaled radio profile is from the second scan of the GBT session on 2009 September 25 (as shown in Figure 1), and the γ-ray profile is the *Fermi* profile accumulated during 2009 September–October. Right: distribution of peak flux density of GPs and energy of γ-ray photons over pulsar rotational phase. The scaled radio profile as for histogram on the left is also shown.

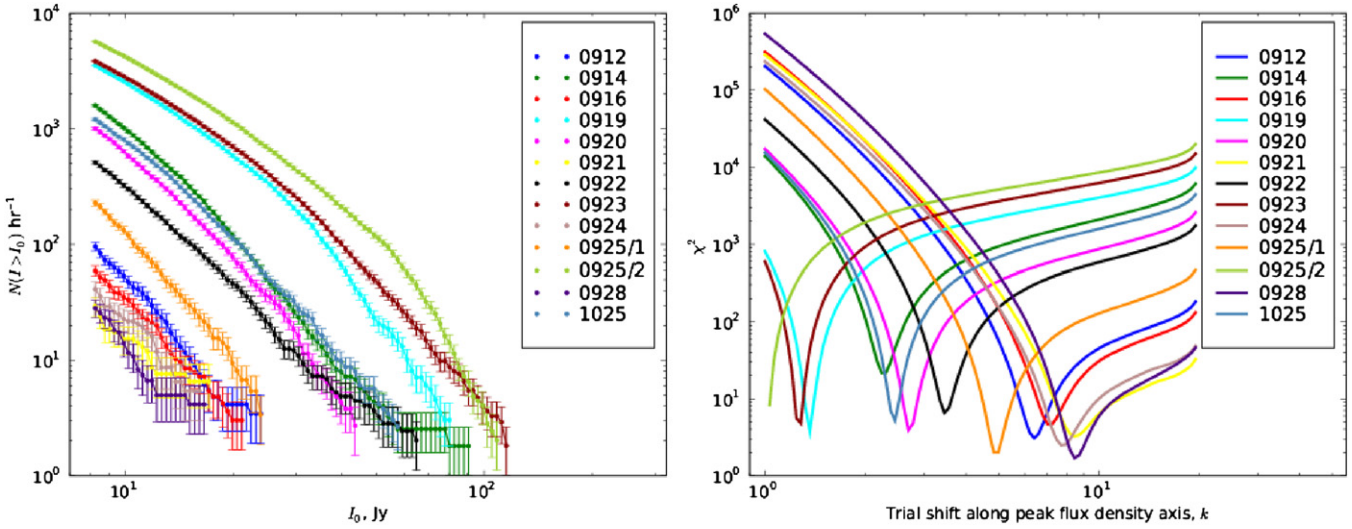

Figure 4. Left: cumulative peak flux distribution of GPs (MP and IP together) for different observing sessions and two subsessions of September 25 with apparently different GP rates. Poisson errors are also shown. Right: χ^2 values vs. the RISS damping coefficient, k, for each observing session.

where $N(I_i)$ is the number of GPs with peak intensity higher than I_i, per hour of observation. $N_{\rm bins}$ is the number of bins in the distributions being compared, and $\sigma_{N(I_i/k)} = \sqrt{N(I_i/k)/T_{\rm hr}}$ is the Poisson error in each bin if $T_{\rm hr}$ is the duration of the session in hours and assuming that the energy of each GP does not depend on the energy of the preceding one.

The χ^2_k curves are plotted in Figure 4 (right). All but one have a sharp minimum of $\chi^2_k \lesssim 10$, indicating reasonable fits, at ks between 1 and 10. The only outlier is the session of September 14, with $\chi^2_{\rm min} = 21.7$, which has an abnormal excess of intrinsically strong GPs (see Figure 2). These GPs do not exhibit any other peculiar properties, other than relatively high peak flux density.

Both RISS coefficients and the corresponding $\chi^2_{\rm min}$ for each day are listed in Table 2. We corrected the session GPs by multiplying their flux densities by k and set the intensity threshold for corrected pulses as 8.1 Jy $\times$ max(k) = 69 Jy (8.1 Jy was our initial threshold, see Section 2).

Thus, we effectively selected only those pulses which would have had peak flux density larger than 8.1 Jy if they were observed during the session with highest RISS damping. Our uniform sample of such intrinsically brightest pulses numbered 180 GPs with TOAs within the *Fermi* observing time.

Table 2
RISS Correction Coefficients k for Each Observing Session

Session	RISS Correction Coefficient k	$\chi^2_{\rm min}$
Sep 12	6.4	3.1
Sep 14	2.2	21.7
Sep 16	7.2	4.7
Sep 19	1.4	3.8
Sep 20	2.7	3.9
Sep 21	8.5	3.3
Sep 22	3.4	6.6
Sep 23	1.3	4.8
Sep 24	7.7	2.5
Sep 25/1	5.0	2.0
Sep 25/2	1.0	0.0
Sep 28	8.5	1.7
Oct 25	2.5	5.2

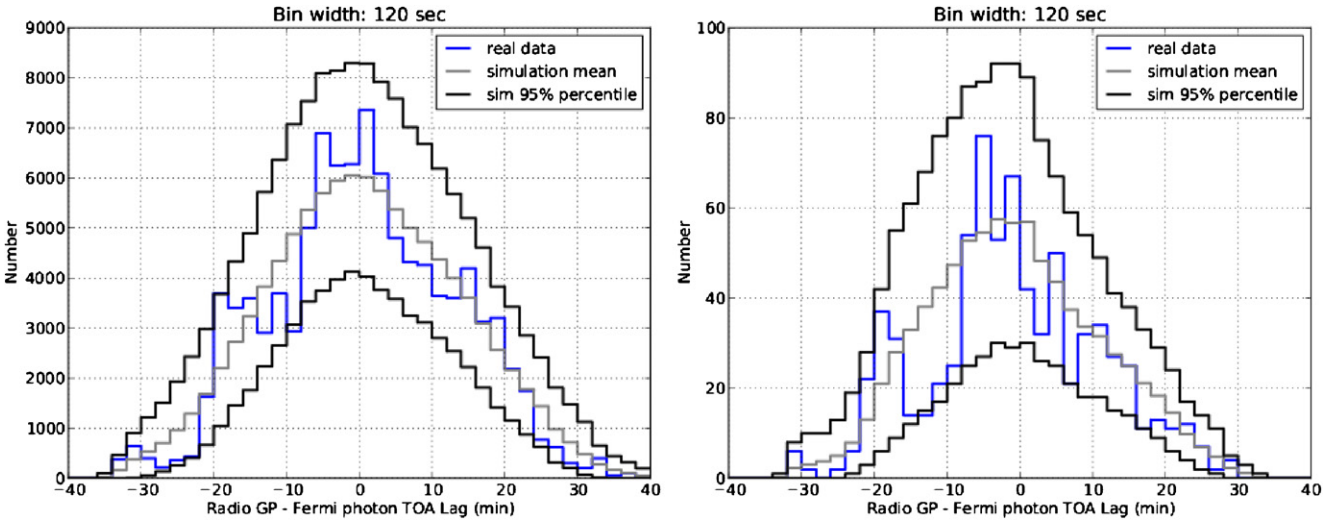

Figure 5. Distribution of time lags between GPs and γ-ray photons for 2 minute bins, for all GPs >8.1 Jy (21,000 GPs; left) and the RISS-corrected GPs (180 GPs; right). Real *Fermi* photons (blue line) are contrasted to the mean and 95% percentile on the pool of simulated data sets (gray and black). The fact that the distribution for the real data lies within 95% of the simulated ones indicates no apparent change in GP generation rate on 2 minute timescale with any possible time lag up to ±40 minutes with respect to the γ-ray photons. The maximum lag value, 40 minutes, corresponds to the size of the largest GTI window. All other bin widths (down to 10 s) give the same result.

5. CORRELATION ANALYSIS

The correlation analysis focused on two distinct tasks. The first one aimed to probe if the GP generation rate correlates with observed γ-ray photons. For the second, we investigated the hypothesis of Lyutikov (2007) that the γ-ray photon flux increases during GPs. For both cases, we used simulated high-energy data sets with no assumed intrinsic correlation between the GPs and γ-ray photons to test the statistical level of correlation present in the real data.

The simulations used the `gtobssim` software from the *Fermi* tools package. We used the latest version of instrument response function, Pass6_v3, together with the same spacecraft/pulsar ephemeris as in real data analysis.

We simulated the pulsar using the `PulsarSpectrum` library, with the light curve, spectrum, and integral flux above 100 MeV taken from Abdo et al. (2010). The integral flux was set to $F_{\rm av} = 2.09 \times 10^{-6}\,{\rm cm}^{-2}\,{\rm s}^{-1}$ for the burst correlation analysis and varied from 0 up to about a hundred $F_{\rm av}$ for the single-pulse correlation analysis (see Section 5.2). When we simulated zero flux from the Crab pulsar, we simply removed the pulsar from the list of simulated sources.

We modeled the Crab Nebula as a point source (for the energy ranges in question, its angular diameter is less than the *Fermi* region of interest), with the spectrum as determined in Abdo et al. (2010) and integral flux above 100 MeV of $9.8 \times 10^{-7}\,{\rm cm}^{-2}\,{\rm s}^{-1}$. For the Galactic and extragalactic backgrounds, we used the "GalacticDiffuse_v02" and "IsotropicDiffuse_v02" models. The simulated photon files were processed in the same way as the real data.

5.1. Is GP Rate Correlated with Single γ-ray Photons?

To test if γ-ray photons are correlated with the GP generation rate, we calculated the distribution of time lags between each photon and all GPs in that photon's GTI. The same procedure was applied to the simulated γ-ray data sets, such that if there were any clustering of GPs around γ-ray photons (or with some time lag with respect to the γ-ray photons), it would be seen as a discrepancy between the real and simulated distributions of the high-energy data. Changing the bin size of the distribution makes it sensitive to different timescales of possible clustering of GPs. In this study, we tried a set of bin widths, starting from 10 s and increasing the width by 10 s up to 2 minutes. Two minutes corresponds to the smallest timescale of GP clumping (likely caused by interstellar scintillation), as shown in Figure 2. On timescales less than 10 s, the Poisson noise due to a discrete number of time lag measurements becomes too high. We performed 1000 simulation runs and contrasted the real-data distribution with the mean and 95% percentile of all of the simulated data sets.

Figure 5 shows the distribution of time lags between GPs and photons for all GPs and for a RISS-corrected sample of GPs for one particular bin width, namely, 2 minutes. In both cases, the real data set lies all within the 95% percentile of the simulations, indicating no apparent change in GP generation rate on 2 minute timescales with any possible time lag within ±40 minutes (maximum GTI length) of the arrival of the γ-ray photons. All other bin widths, down to 10 s, gave the same result.

5.2. Does γ-ray Flux Change around Single GPs?

Another question of interest is whether the average γ-ray flux from the Crab pulsar increases during individual GPs, as predicted by Lyutikov (2007). To investigate that we looked for the number of γ-ray photons in on-pulse emission windows around each GP. We performed a separate search for all GPs, looking for photons in a large window consisting of the MP, IP and bridge between them, and also for IP GPs only, limiting the correlation window to the IP phase range.

If a photon was detected in a window around a GP, it was called a "match." For 10.5 hr of simultaneous observations, *we detected only one such match*: a photon with $E = 403.7$ MeV was detected within 1.3 ms of IP GP with peak flux density of 8.9 Jy. Nonetheless, knowing the observed number of matches $N = 1$, the probability that the γ-ray flux during GPs is equal to some value F_0 can be estimated with the simple Bayesian formula:

$$p(F = F_0|N) = \frac{p(F_0) \cdot p(N|F = F_0)}{\int_0^{F_{\rm max}} p(F_0) \cdot p(N|F = F_x) dF_x}, \quad (2)$$

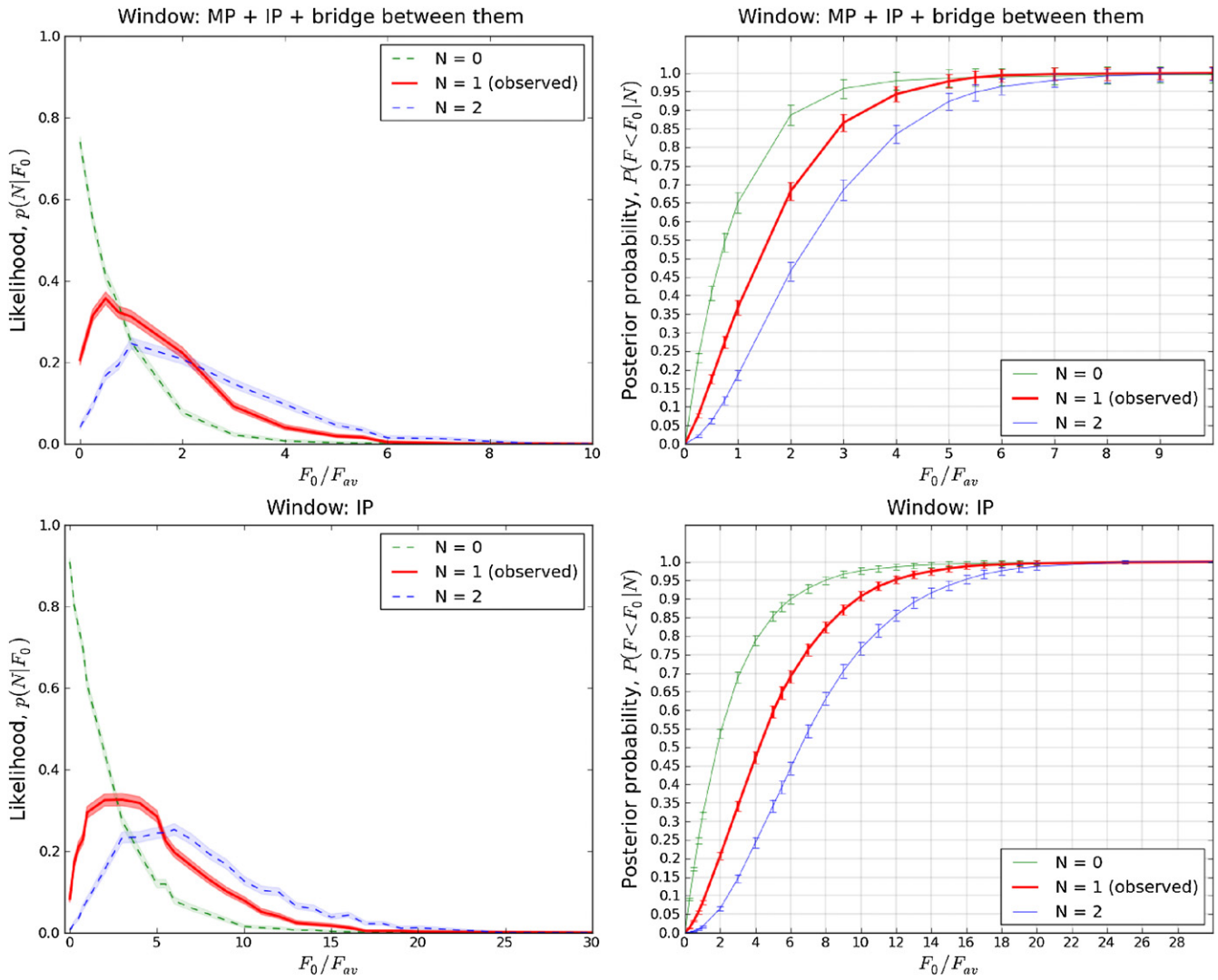

Figure 6. Left: likelihood, the probability of observing N photons in a certain window around a GP if the γ-ray flux from the pulsar in this window were F_0. For each window size, we observed only one such match between GP and γ-ray photon, so $N = 1$. Since photon arrival times are a Poisson process, the error on N is $\sqrt{N} = 1$, thus likelihood curves for $N = 0$ and $N = 2$ are also shown. The shaded region around each curve corresponds to uncertainty due to the limited number of simulation runs (see the text for explanation). Both $N = 1$ likelihood curves peak near $F_0/F_{\rm av} = 1$, so no or weak correlation between GPs and γ-ray photons is the most probable. Right: posterior probability that γ-ray flux in a window around GP is less than F_0, given the observed number of matches N. Errors due to the limited number of simulation runs are plotted as error bars, whereas those due to a discrete number of matches are given by separate posterior probability curves for $N = 0$ and $N = 2$. $F_{\rm av}$, the average pulsed γ-ray flux from Crab pulsar, is from Abdo et al. (2010).

where $p(F_0)$ is the prior distribution for F_0 and $p(N|F = F_0)$ is the likelihood, i.e., the probability to get the observed number of matches N if the pulsar γ-ray flux during GPs is equal to F_0.

Since little is known about $p(F_0)$, the prior distribution for F_0, we chose the prior to be uniform in a flux range from 0 (the Crab pulsar turns off γ-ray emission during GPs) to

$$F_{\rm max} \equiv F_{\rm av} \frac{\text{observing timespan}}{N_{\rm GP} \times \text{ length of window}}, \quad (3)$$

where $F_{\rm av}$ is the average pulsed γ-ray flux from the Crab pulsar. $F_{\rm max}$ corresponds to the hypothesis that all γ-ray photons from the Crab pulsar come during GPs. For our choice of windows, $F_{\rm max}$ ranged from 60 $F_{\rm av}$ (for on-pulse phase window) to 150 $F_{\rm av}$ (for IP window).

The likelihood $p(N|F = F_0)$ was calculated by running simulations with different pulsed flux F_0 and computing the fraction of runs with a number of matches N. The grid of trial flux values, in units of $F_{\rm av}$, was as follows: from 0 to 1 with the step of 0.25, from 1 to 20 with the step of 1 or 0.5, and then from 20 to 30 with the step of 5. For both choices of correlation window, the probability density went down to 0 before 30 $F_{\rm av}$. Here we implicitly assumed that a higher flux outside selected windows does not influence the correlation within windows.

Since the number of simulation runs for each trial F_0 is finite, it leads to an uncertainty in estimating the likelihood. We estimated the statistical errors from the simulation using the following method. Suppose that for some value of F_0 we have run n simulations with y successes (i.e., cases where the number of matches in the simulation equals the one obtained for real data, N). Then, y/n defines the estimate of probability of success p, which is also the likelihood density $p(N|F = F_0)$. More precisely, $p|y$ has a Beta distribution, with mean $(y+1)/(n+1)$ and variance $\sigma_p^2 = \frac{(y+1)(n-y+1)}{(n+3)(n+2)^2}$. We adopted σ_p as an error of p due to limited numbers of simulations performed.

However, there is another major source of uncertainty connected to the fact that we record a discrete number of photons around the GPs. Since photon detection is very well described as a Poisson process (Ramanamurthy & Thompson 1998), the

error on detecting N photons in a certain window around GPs will be $\sqrt{N}$. In our case, for all windows we had $N = 1$, so to estimate the true value of the likelihood we should also take into consideration the likelihood curves for $N = 0$ and $N = 2$. These estimates for both windows are plotted in Figure 6, left. The shaded region around each curve corresponds to $\pm\sigma_p$, calculated by the above formula. For both correlation windows $N = 1$ likelihood curves have maximum around $F_0/F_{\rm av} = 1$, which means that, most probably, pulsed γ-ray flux does not change during GPs (no correlation) or changes no more than a few times (weak correlation).

With our limited data set, we cannot say anything more about the exact value of γ-ray flux during GPs, but we can place upper limits on it. On the grid of simulated fluxes F_i, one can convert the continuous formula for posterior probability density (Equation (2)) into a discrete one for the probability that pulsed flux around GPs is *less* than F_0:

$$P(F \leqslant F_0|N) = \frac{0.5 \cdot \sum_{F_{i+1} \leqslant F_0} (p_i + p_{i+1})(F_{i+1} - F_i)}{0.5 \cdot \sum (p_i + p_{i+1})(F_{i+1} - F_i)}, \quad (4)$$

where $p_i \equiv p(N|F = F_i)$.

To estimate errors in $P(F \leqslant F_0|N)$, we assumed that our uncertainty in p_i due to a limited number of trials is much larger than the error from calculating the integral as a sum. As one can see in Figure 6, left, this simplification is reasonable. Assuming all σ_{p_i} are independent, the uncertainty in $P(F \leqslant F_0|N)$ is determined by standard error propagation.

In Figure 6, we show the resulting probabilities that the γ-ray flux from the Crab pulsar during GPs does not exceed a given number of times the mean flux reported by Abdo et al. (2010). Errors due to the limited number of simulation runs are plotted as error bars, whereas those due to a discrete number of GP/photon matches are given by separate posterior probability curves for $N = 0$ and $N = 2$.

Obviously, the smaller the correlation window for a fixed observation timespan and the smaller the number of GPs in the sample, the larger $F_{\rm max}$, and the broader is the resulting posterior probability density. That is why for our data set we could obtain the posterior probability densities only for correlation windows which included the IP, because most of GPs come within this phase range. For the MP GPs, $p(F = F_0|N)$ is very broad, having almost the same probability density up to $\sim$100 $F_{\rm av}$. For the same reasons, the analysis on the sample of GPs corrected for refractive scintillation did not give any meaningful results.

6. CONCLUSIONS

No obvious correlation was found between *Fermi* photons of energies >100 MeV and radio GPs at the frequency of 8.9 GHz. No change in the Crab GP generation rate was found on timescales from 10 to 120 s around γ-ray photons and with any possible lag within $\pm$40 minutes with respect to γ-ray photons.

With 95% probability, the high-energy flux of the Crab pulsar during GPs is less than four times the average γ-ray pulsed flux for the on-pulse (MP+IP+bridge between them) phase window. For IP GPs only, the 95% upper limit on γ-ray flux in the IP phase window is 12 times the average pulsed flux. If we consider the uncertainty due to discrete numbers of matches between photons and GPs, the 95% upper limits are 3–5.5 times the average pulsed flux for the pulsed emission window and 8–16 for the IP window.

A few explanations may be offered for the non-detection of GP–γ-photon correlations. The most natural is that production of GPs depends on non-stationary changing coherence conditions, which vary by a large degree even for similar magnetospheric particle densities. Another possibility is that beaming in radio and at high energies are somewhat different, so that simultaneous GPs and γ-ray photons are emitted in different directions.

Overall, our results suggest that enhanced pair creation is not a dominant factor for GP occurrence, at least for high-frequency IP GPs. However, our flux increase estimations are not on the level of a few percent, as in the work of Shearer et al. (2003) at optical wavelengths. To reach that sensitivity we need more data, which will help push down the upper limit on flux during GPs and will make possible the analysis on subsamples of GPs, such as the brightest ones. Also, including radio frequencies below 4 GHz is potentially interesting not only for investigating the correlation for MP GPs separately (MP GPs are much more common at lower frequencies) but also for re-doing the analysis for low-frequency IP GPs, since they might be generated by different physical processes than the high-frequency IP GPs (Moffett 1997). All these questions are being investigated with our ongoing radio observation campaign using the 42 ft telescope at the Jodrell Bank Observatory (UK) and the 140 ft telescope at the Green Bank Observatory (WV).

The National Radio Astronomy Observatory is a facility of the National Science Foundation operated under cooperative agreement by Associated Universities, Inc. This work was supported by *Fermi* grant NNX10AD14G. M.A.M. is an Adjunct Astronomer at the National Radio Astronomy Observatory and is supported by a Cottrell Fellowship, a Sloan Fellowship, and a WVEPSCOR Research Challenge Grant. A.V.B. thanks T. T. Pennucci (UVa) for the useful comments on the paper draft.

REFERENCES

Abdo, A. A., et al. 2010, ApJ, 708, 1254
Cordes, J. M., Bhat, N. D. R., Hankins, T. H., McLaughlin, M. A., & Kern, J. 2004, ApJ, 612, 375
Cusumano, G., et al. 2003, A&A, 410, L9
Ginzburg, V. L. 1985, in Physics and Astrophysics: A Selection of Key Problems, ed. V. L. Ginzburg (Oxford, NY: Pergamon), 139
Hankins, T. H., Kern, J. S., Weatherall, J. C., & Eilek, J. A. 2003, Nature, 422, 141
Herfindal, J. L., & Rankin, J. M. 2009, MNRAS, 393, 1391
Hobbs, G. B., Edwards, R. T., & Manchester, R. N. 2006, MNRAS, 369, 655
Jessner, A., Słowikowska, A., Klein, B., Lesch, H., Jaroschek, C. H., Kanbach, G., & Hankins, T. H. 2005, Adv. Space Res., 35, 1166
Knight, H. S., Bailes, M., Manchester, R. N., Ord, S. M., & Jacoby, B. A. 2006, ApJ, 640, 941
Kramer, M., Lyne, A. G., O'Brien, J. T., Jordan, C. A., & Lorimer, D. R. 2006, Science, 312, 549
Lundgren, S. C. 1994, PhD thesis, Cornell Univ., Ithaca, NY
Lundgren, S. C., Cordes, J. M., Ulmer, M., Matz, S. M., Lomatch, S., Foster, R. S., & Hankins, T. 1995, ApJ, 453, 433
Lyutikov, M. 2007, MNRAS, 381, 1190
Lyutikov, M., Blandford, R. D., & Machabeli, G. 1999, MNRAS, 305, 338
Machabeli, G. Z., & Usov, V. V. 1979, Sov. Astron. Lett., 5, 238
McLaughlin, M. A., et al. 2006, Nature, 439, 817
Moffett, D. A. 1997, PhD thesis, New Mexico Inst. Mining and Technology
Moffett, D. A., & Hankins, T. H. 1996, ApJ, 468, 779
Popov, M. V., & Stappers, B. 2007, A&A, 470, 1003
Popov, M. V., Soglasnov, V. A., Kondrat'ev, V. I., Kostyuk, S. V., Ilyasov, Yu. P., & Oreshko, V. V. 2006, Astron. Rep., 50, 55 (transl. from 2006, AZh, 83, 630)
Ramanamurthy, P. V., & Thompson, D. J. 1998, ApJ, 496, 863
Rickett, B. J., & Lyne, A. G. 1990, MNRAS, 244, 68
Shearer, A., Stappers, B., O'Connor, P., Golden, A., Strom, R., Redfern, M., & Ryan, O. 2003, Science, 301, 493
Staelin, D. H., & Reifenstein, E. C., III. 1968, Science, 162, 1481